

Title: Electrically tunable moiré magnetism in twisted double bilayer antiferromagnets

Guanghui Cheng^{1,2,3,4,12}, Mohammad Mushfiqur Rahman^{5,12}, Andres Llacahuanga Allecca^{1,2,6}, Avinash Rustagi⁵, Xingtao Liu^{1,7}, Lina Liu^{1,2}, Lei Fu^{1,2}, Yanglin Zhu⁸, Zhiqiang Mao⁸, Kenji Watanabe⁹, Takashi Taniguchi¹⁰, Pramey Upadhyaya^{2,5,6*}, Yong P. Chen^{1,2,4,5,6,11*}

¹Department of Physics and Astronomy, and Birck Nanotechnology Center, Purdue University; West Lafayette, Indiana 47907, USA.

²Purdue Quantum Science and Engineering Institute, Purdue University; West Lafayette, Indiana 47907, USA.

³Department of Physics, University of Science and Technology of China; Hefei, Anhui 230026, China.

⁴WPI-AIMR International Research Center for Materials Sciences, Tohoku University; Sendai 980-8577, Japan.

⁵School of Electrical and Computer Engineering, Purdue University; West Lafayette, Indiana 47907, USA.

⁶Quantum Science Center; Oak Ridge, Tennessee 37831 USA.

⁷School of Industrial Engineering, Purdue University, West Lafayette, Indiana 47907, USA.

⁸Department of Physics, Pennsylvania State University; University Park, Pennsylvania 16802, USA.

⁹Research Center for Functional Materials, National Institute for Materials Science; 1-1 Namiki, Tsukuba 305-0044, Japan.

¹⁰International Center for Materials Nanoarchitectonics, National Institute for Materials Science; 1-1 Namiki, Tsukuba 305-0044, Japan.

¹¹Institute of Physics and Astronomy and Villum Centers for Dirac Materials and for Hybrid Quantum Materials, Aarhus University; 8000 Aarhus-C, Denmark.

¹²These authors contributed equally: Guanghui Cheng, Mohammad Mushfiqur Rahman.

*Corresponding authors. Emails: prameyup@purdue.edu; yongchen@purdue.edu

Abstract: The introduction of moiré superlattices to electronic materials can dramatically alter electronic properties, promising emergent correlated and topological phenomena. Its first demonstration in van der Waals magnets exhibited noncollinear states and domain structures with, however, limited manipulation. Here, we fabricated twisted double antiferromagnetic bilayer CrI₃, and by magneto-optical Kerr effect microscopy demonstrate the coexistence of antiferromagnetic and ferromagnetic orders with nonzero net magnetization, which is the hallmark of moiré magnetism. Such magnetic state exhibits nonmonotonic temperature dependence and extends over a wide range of twist angles with transitions at $\sim 0^\circ$ and above 20° . We further demonstrate voltage-assisted magnetic switching and the linear magnetoelectric effect. The observed nontrivial magnetic states and unprecedented control by twist angle, temperature and electrical gating are supported by the simulated phase diagram of the moiré magnetism. Our results illustrate the rich behaviors of twisted antiferromagnets and the control over them.

Moiré superlattices have shown the potential for exploring and controlling a wealth of quantum phases¹⁻¹³, by simply stacking one layer of van der Waals (vdW) material onto another layer with either lattice mismatch or a small twist angle. Such a large super-periodic pattern defines a new crystal structure with electronic bands folded into a mini-Brillouin zone, capable of forming flat bands and driving the system to strongly correlated regimes. A plethora of remarkable properties, such as superconductivity, Mott insulating states, and moiré excitons, have emerged in twisted graphene, transition metal dichalcogenides, and other electronic materials^{1-6, 8, 13}. Such tremendous control over the charge degree of freedom has made moiré superlattices versatile electronic quantum simulators and platforms to discover novel phases of matter. It is highly desired to further expand such explorations to additional material types and (beyond charge) degrees of freedom.

The advent of vdW magnets is of particular interest due to novel two-dimensional magnetic phenomena as well as the versatile manipulation of the spin degree of freedom¹⁴⁻²⁰. Recent theoretical works have predicted twisted bilayers of vdW magnets to host exotic magnetic phases²¹⁻²⁴. Noncollinear spin textures, topological skyrmion lattices, and rich spectra of magnonic subbands can emerge from the modulation of interlayer exchange interactions in the presence of moiré superlattices²¹⁻²⁴. One promising candidate is based on the layered antiferromagnet CrI₃. In particular, the interlayer magnetic exchange of bilayer CrI₃ depends on the structural stacking orders^{18, 25}, where monoclinic stacking favors antiferromagnetic (AFM) coupling and rhombohedral stacking favors ferromagnetic (FM) coupling. Under rigid rotation, twisting one CrI₃ layer relative to another layer can create a moiré superlattice with rhombus-shaped primitive cells (Fig. 1a). The atomic registry varies continuously, leading to alternating structural domains: AA stacking (top and bottom Cr atoms are aligned vertically), rhombohedral stacking, and monoclinic stacking. Therefore, the stacking-dependent interlayer exchange in twisted CrI₃ can give rise to magnetic domains and noncollinear spin textures. Recently, such coexisting AFM/FM states have been experimentally demonstrated in twisted CrI₃ by magneto-optical measurements and Raman spectroscopy^{11, 12}, and the nanoscale magnetic domains are visualized by quantum magnetometry¹⁰. These discoveries highlight twisted vdW magnets as potential platforms to explore and engineer nontrivial magnetic phases with novel spin degrees of freedom. However, many aspects of the predicted and rich varieties of noncollinear spin states remain to be experimentally elucidated and the effective manipulation of moiré magnetism, e.g., magnetization reversal by electrical methods^{17, 26, 27}, has also yet to be demonstrated.

In this work, we explore the magnetism of twisted double bilayer CrI₃ (tDB CrI₃), i.e., bilayer plus bilayer with a twist angle between them. We show the coexistence of antiferromagnetic and ferromagnetic orders tuned by the twist angle, the nonmonotonic temperature dependence of magnetization, and the electrical control over the magnetic states, which are supported by the proposed phase diagram of moiré magnetism. We fabricated tDB CrI₃ by the tear-and-stack technique^{13, 28} in an argon glovebox and encapsulated it with hexagonal boron nitride (hBN) flakes (Methods). The atomic force microscopy image (Supplementary Section 1) suggests a uniform stacking interface with few bubbles. We employ magneto-optical Kerr effect microscopy (MOKE) under polar configuration as the primary measurement due to its high sensitivity to the magnetic moments perpendicular to the sample surface²⁹. All MOKE measurements were performed under a perpendicular magnetic field at 6 K unless otherwise specified (Methods).

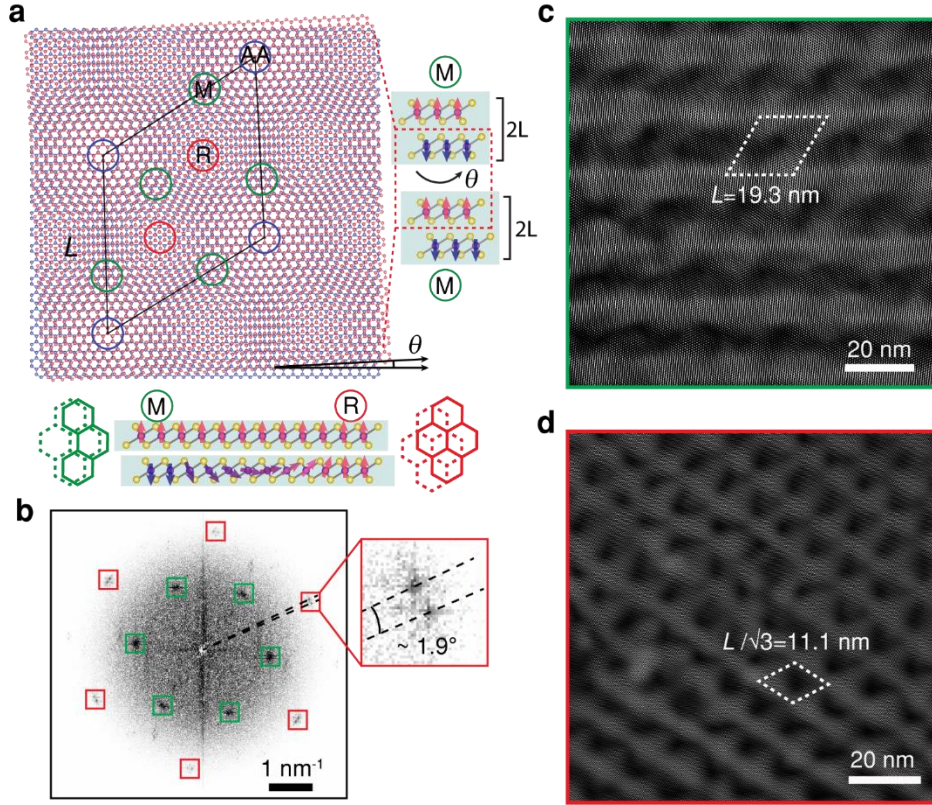


Figure 1 | Moiré superlattice and STEM characterizations of tDB CrI₃. **a**, The moiré superlattice structure of tDB CrI₃ with a twist angle θ between the two bilayers. Only Cr atoms of the middle two CrI₃ layers are shown for simplicity with red and blue balls belonging to each of the two layers. Regions of AA stacking, monoclinic (M) stacking, and rhombohedral (R) stacking are indicated by blue, green and red circles, respectively. The rhombus-shaped lines indicate the moiré primitive cell with a period of L . Right: The middle two layers of tDB CrI₃ are twisted, and the top/bottom CrI₃ bilayers ($2L$) retain monoclinic stacking. Bottom: Noncollinear spin textures of the monoclinic-rhombohedral domain wall formed in the twisted middle two layers. **b**, FFT pattern of the STEM image (Supplementary Section 2) of a tDB CrI₃ with a target twist angle of 1.42° . Green and red rectangles mark the first- and second-order Bragg peaks, respectively. Right: The magnification of one peak shows two slightly separated peaks from the top and bottom bilayer CrI₃ with a measured twist angle of $\sim 1.9^\circ$. **c,d**, Real-space moiré patterns reconstructed by inverse FFT of the two sets of Bragg peaks marked by green and red rectangles respectively in **b**. Rhombus-shaped lines indicate primitive cells with periods related to moiré wavelength L .

We employ high-angle annular dark-field scanning transmission electron microscopy (STEM) to characterize the moiré superlattice of tDB CrI₃ (Methods). Figure 1b shows the fast Fourier transform (FFT) of the STM image of a tDB CrI₃ with a target twist angle of 1.42° (see the original STEM images in Supplementary Section 2). Two sets of first- and second-order Bragg peaks with sixfold rotation symmetry are marked by the green and red rectangles. A close inspection of one representative peak reveals two slightly separated peaks corresponding to the top and bottom bilayer CrI₃. As a comparison, no splitting is observed for the Bragg peaks of the natural bilayer CrI₃ (Supplementary Section 2). From the splitting, we can measure the actual twist angle to be $\sim 1.9^\circ$, within the accuracy of $\sim \pm 0.5^\circ$ of the stacking processes. Such a twisted-angle accuracy is comparable with that in other works¹⁰⁻¹². In this paper, unless otherwise specified, all twist angles (denoted θ) of the experimental samples refer to the target twist angles. The moiré wavelength³⁰ can be estimated to be $L = \frac{a}{2 \sin(\theta/2)}$, where a is the lattice constant of CrI₃²⁴, and is ~ 20.5

nm for the above sample. By inverse FFT of the two sets of Bragg peaks marked by green and red rectangles in Fig. 1b, the real-space moiré patterns are reconstructed in Figs. 1c,d, corresponding to the first and second orders of the moiré superlattice. Both pattern periods are consistent with the expectations L and $L/\sqrt{3}$ based on the moiré wavelength. The STEM characterizations demonstrate the formation of a moiré superlattice in tDB CrI₃.

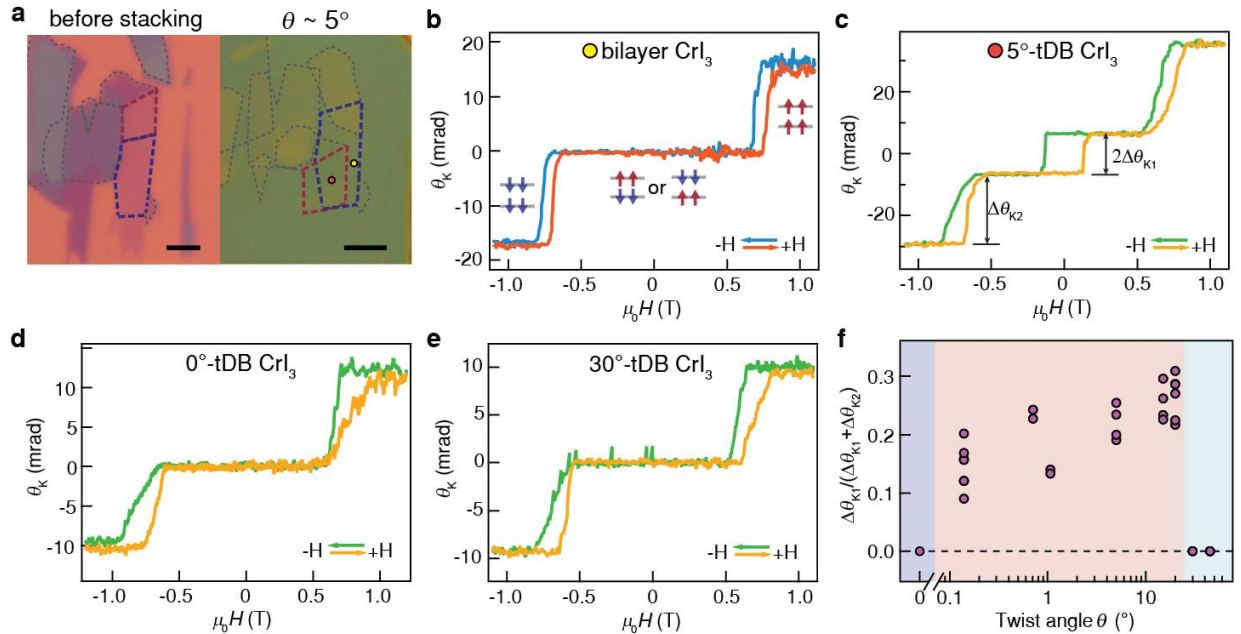


Figure 2 | Twist angle dependence of the magnetic behaviors in tDB CrI₃. **a**, Optical micrograph of a bilayer CrI₃ flake (left) and a 5°-tDB CrI₃ (right) made from it by the tear-and-stack technique. The top and bottom bilayers CrI₃ are outlined by the blue and red dashed lines, respectively. Thicker flakes are outlined by gray dashed lines. Scale bars are 5 μm . **b,c**, MOKE signal as a function of perpendicular magnetic field in bilayer CrI₃ and 5°-tDB CrI₃ (both from the same CrI₃ flake), measured at the yellow and red spots in **a**, respectively. Magnitudes of the FM loop and AFM spin-flip transition are denoted by $\Delta\theta_{K1}$ and $\Delta\theta_{K2}$. Insets in **b** depict the magnetic ground states of bilayer CrI₃. **d,e**, MOKE signal as a function of magnetic field in 0°- and 30°-tDB CrI₃. **f**, Fraction of MOKE magnitudes $\Delta\theta_{K1}/(\Delta\theta_{K1}+\Delta\theta_{K2})$ as a function of the twist angle (θ , in log scale). The data points at each angle are measured at different positions of each sample. Data (zero value) at θ of 0°, 30°, and 45° each have at least two reproducible points overlapping. Blue-, pink- and cyan-shaded areas are the guide to the eyes. The twist angle accuracy is $\sim 0.5^\circ$.

Figure 2a shows the optical micrograph of a representative bilayer CrI₃ flake (left) and a 5°-tDB CrI₃ (right) made from it. The MOKE signals as a function of magnetic field in bilayer CrI₃ and 5°-tDB CrI₃ are shown in Figs. 2b,c, measured at the yellow and red spots in Fig. 2a, respectively. In the bilayer CrI₃ region, we observed zero magnetization at zero field and sharp jumps at fields of ± 0.7 T, consistent with the reported AFM spin-flip transition in the natural bilayer CrI₃^{31,32}. We denote all spins in each layer by a macroscopic spin (out-of-plane: \uparrow, \downarrow ; in-plane: \leftarrow, \rightarrow). The magnetic ground states are shown in the insets.

In stark contrast, within the tDB CrI₃ region, in addition to the AFM spin-flip transitions present at fields of $\sim \pm 0.7$ T (analogous to those in bilayer CrI₃), a new and significant *FM hysteresis loop* emerges with transition fields of $\sim \pm 0.2$ T. In comparison, the MOKE results of natural four-layer CrI₃ suggest interlayer AFM coupling without an FM loop³² (Supplementary Section 3). For tDB CrI₃, the assumption of AFM spin orientations within each of the top and bottom bilayers breaks down, since it leads to zero net magnetization regardless of the coupling type between the middle two layers. Here, we propose that the

observed AFM and FM behaviors in tDB CrI₃ are due to the coexistence of AFM/FM domains predicted for moiré magnetism^{21,23}, similar to the reported magnetic domains in twisted bilayer CrI₃¹⁰⁻¹².

The moiré magnetism is essentially determined by competing magnetic interactions dependent on the twist angle^{21,24}. We thus studied the twist angle dependence of the magnetic behaviors in tDB CrI₃. Figures 2d,e show the MOKE results in 0°- and 30°-tDB CrI₃, respectively (0°-tDB CrI₃ refers to stacking bilayer on bilayer with 0°, instead of a natural four-layer CrI₃). Only AFM spin-flip transitions are present, while the FM loop disappears, in sharp contrast to 5°-tDB CrI₃. Data from other samples with additional twist angles are shown in Supplementary Section 4. Furthermore, MOKE results of a representative tDB CrI₃ sample exhibiting both FM loop and AFM spin-flip transitions show no other transitions up to higher fields of ± 2 T (Supplementary Section 5), indicating the fully polarized spin states at fields larger than 0.7 T. We denote the magnitudes of the FM loop and AFM spin-flip transition as $\Delta\theta_{K1}$, $\Delta\theta_{K2}$ and summarize the FM fraction $\Delta\theta_{K1}/(\Delta\theta_{K1}+\Delta\theta_{K2})$ as a function of the twist angle in Fig. 2f. The data points at each twist angle are obtained at different positions of each sample (see uniformity check in Supplementary Section 6). The nonzero fractions (reaching maximum value ~ 0.3) in the twist angle range of $0.14^\circ - 20^\circ$ indicate a regime with coexisting FM and AFM behaviors. The FM loop disappears for twist angles of $\sim 0^\circ$ or above 20° , suggesting phase transitions across critical angles. Such systematic twist angle dependence and reproducible results support the noncollinear moiré magnetism emerging in tDB CrI₃. The possible noncollinear phases will be discussed with the theoretically calculated phase diagram shown later. We further plot another quantity, the transition fields of both FM coercivity and AFM spin-flip, as a function of the twist angle in Supplementary Section 7. No significant dependence is observed, suggesting that the magnetic anisotropy in this system is hardly tuned by the moiré superlattice.

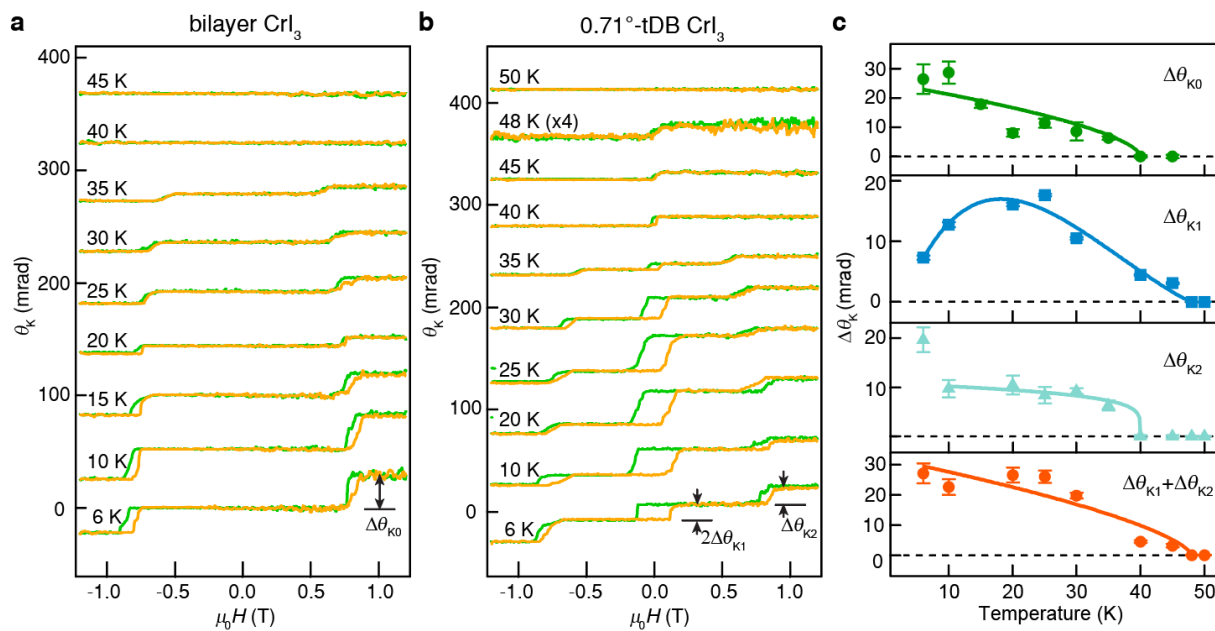


Figure 3 | Temperature dependence of the magnetic behaviors in tDB CrI₃. a,b, MOKE signal as a function of magnetic field at representative temperatures in bilayer CrI₃ and 0.71°-tDB CrI₃ (from the same bilayer CrI₃ flake), respectively. Curves are vertically shifted for clarity. c, MOKE magnitudes of the bilayer AFM spin-flip transition $\Delta\theta_{K0}$, the tDB FM loop $\Delta\theta_{K1}$, the AFM spin-flip transition $\Delta\theta_{K2}$ and the total magnitude $\Delta\theta_{K1} + \Delta\theta_{K2}$ as functions of temperature extracted from a,b. Solid lines are phenomenological fits with the power-law form, as the guide to the eyes. The error bars are the uncertainties in extracting the MOKE magnitudes.

We further investigate the temperature dependence of the magnetic behaviors. Figures 3a,b show the MOKE results for bilayer CrI₃ and 0.71°-tDB CrI₃ at various temperatures. With increasing temperature, the FM coercivity and AFM spin-flip transitions occur at lower fields and with reduced MOKE amplitudes, eventually disappearing at 40 ~ 50 K, consistent with the studies in natural bilayer CrI₃ and twisted bilayer CrI₃^{11, 17, 31}. Careful inspection reveals that the critical temperature of the FM coercivity is somewhat higher than that of the AFM spin-flip transition, perhaps due to the effective anisotropy field introduced by the interfacial exchange coupling^{20, 33}, which needs further studies to fully understand. Figure 3c shows the MOKE magnitudes of the AFM spin-flip transition $\Delta\theta_{K0}$ in natural bilayer, and the FM loop $\Delta\theta_{K1}$, the AFM spin-flip transition $\Delta\theta_{K2}$ and the total magnitude $\Delta\theta_{K1} + \Delta\theta_{K2}$ in tDB as functions of temperature extracted from Figs. 3a,b. Remarkably, $\Delta\theta_{K1}$ of 0.71°-tDB CrI₃ (proportional to the net out-of-plane magnetization within the noncollinear phase) first increases and then drops down with increasing temperature. In contrast, $\Delta\theta_{K0}$ of bilayer CrI₃ and $\Delta\theta_{K2}$, $\Delta\theta_{K1} + \Delta\theta_{K2}$ of 0.71°-tDB CrI₃ (proportional to the saturation magnetization of the sample, M_s) monotonically decrease with increasing temperature, typical of magnets making a transition from a ferromagnetic phase to a paramagnetic phase. As discussed below, the anomalous nonmonotonic behavior of $\Delta\theta_{K1}$ is further consistent with the presence of noncollinear phases. Namely, it can be qualitatively understood as the temperature-induced crossover between noncollinear phases arising from different power-law dependences of the magnetic parameters (anisotropy K , interlayer exchange J_{\perp}^0 and intralayer exchange A) on the temperature^{11, 34, 35}.

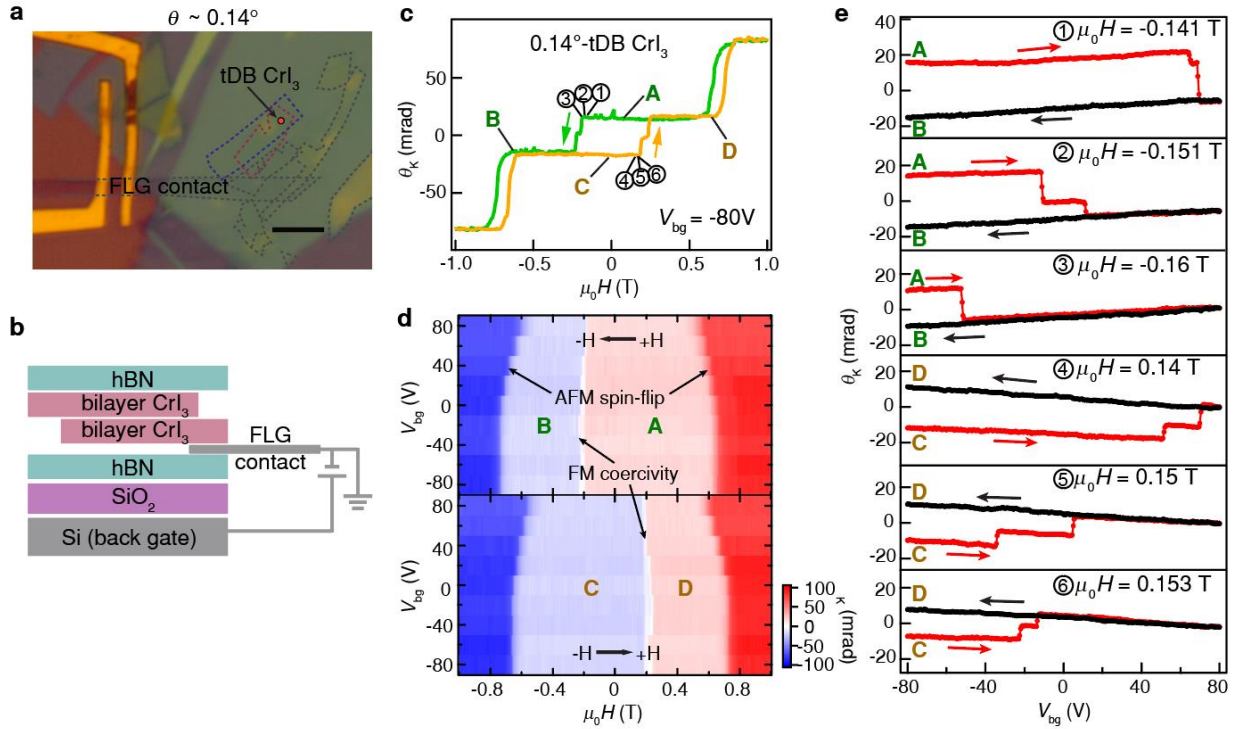


Figure 4 | Electrical control of the magnetic behaviors in tDB CrI₃. **a,b**, Optical micrograph ($\theta \sim 0.14^\circ$) and schematic side view of a back-gated tDB CrI₃ device. A few-layer graphene (FLG) flake is used as the contact to the stack. **c**, MOKE signal as a function of magnetic field at a gate voltage of -80 V. Field sweeping directions are denoted by the arrows. Four plateaus at low fields are denoted by A, B, C and D. **d**, MOKE signal as a function of magnetic field and back-gate voltage. The top and bottom panels correspond to backward and forward sweeps of the magnetic field, respectively. The sharp color boundaries marked by arrows indicate the FM coercivity and AFM spin-flip transitions. **e**, Gate-voltage-controlled magnetic switching. Voltage sweeping directions are denoted by the arrows. The sample is initialized in the fully polarized states by a high magnetic field of +(-)1T and then biased at fields of

① -0.141 T, ② -0.151 T, ③ -0.16 T, (④ 0.14 T, ⑤ 0.15 T, ⑥ 0.153 T), respectively, corresponding to the circled numbers in **c**. The intermediate states (minor plateaus) seen in **c** and **e** during A-to-B and C-to-D switchings may be due to magnetic domains and are not the focus of this study.

We next explore the electrical control of the magnetic behaviors in tDB CrI₃. We fabricated a back-gated 0.14°-tDB CrI₃ device (Methods), as shown in Figs. 4a,b. The MOKE results at a gate voltage of -80 V (Fig. 4c) present the coexistence of AFM and FM transitions, the same feature as discussed above for noncollinear moiré magnetism. Four plateaus at low fields representing distinct magnetic states are denoted by A, B, C and D (presumably with positive, negative, negative and positive magnetization respectively, with the MOKE signal sign consistent with the correspondingly polarized state at high fields). Figure 4d shows the MOKE signal as a function of the magnetic field at various back-gate voltages (see representative MOKE curves in Supplementary Section 8). The top and bottom panels correspond to backward and forward sweeps of the magnetic field, respectively. The sharp color boundaries represent FM coercivity and AFM spin-flip transitions. Both occur at lower magnetic fields with increasing back-gate voltage, suggesting a high electrical tunability of the magnetic anisotropy and interlayer exchange. Similar electric tunability is observed in natural bilayer CrI₃^{17, 27, 36}, which is associated with doping-modulated interlayer exchange coupling.

Remarkably, we observed voltage-controlled magnetic switching in tDB CrI₃. Such switching is essentially due to the electrical modulation of coercive fields. Here, we biased the magnetic field close to the FM coercive field denoted by the circled numbers in Fig. 4c. The corresponding MOKE signal as a function of back-gate voltage V_{bg} is shown in Fig. 4e. At a fixed voltage $V_{bg} = -80$ V, the tDB CrI₃ sample is first initialized in the fully polarized state by applying a high magnetic field of 1 T and then biased at a field of -0.141 T (trace 1), corresponding to a noncollinear ground state (A state, with positive magnetization). When sweeping V_{bg} from -80 V to 80 V, an abrupt switching to the B state occurs at ~70 V. For biased fields of -0.151 T (trace 2) and -0.16 T (trace 3), which are still higher but closer to the coercive field (-0.178 T) at $V_{bg} = -80$ V, switching occurs at earlier voltages of -10 V and -50 V, respectively. This is consistent with the trend of decreasing coercive field magnitude for more positive V_{bg} (Fig. 4d and Fig. S8) for this sample. However, the system stays at the B state when sweeping the voltage backward, presumably because the B state with negative magnetization is the low-energy state under the negative magnetic field, and an energy barrier prevents the system from returning to the A state. Such one-time magnetic switching has also been reported in other ferromagnetic systems^{27, 37}. Conversely, for the initialization by a negative high field of -1T and biased fields of 0.14 T, 0.15 T, 0.153 T (traces 4, 5, 6, increasingly close to the coercive field of 0.174 T at $V_{bg} = -80$ V for the forward magnetic field sweep), voltage-controlled switching is observed from a noncollinear state with negative magnetization (C state) to that with positive magnetization (D state). The voltage-assisted switching is also observed in other tDB CrI₃ samples with twist angles of 5° and 20° (Supplementary Section 9).

Besides voltage-assisted switching, we further observed a linear dependence of the MOKE signal on the voltage with a positive slope for traces 1, 2, and 3 in Fig. 4e. This suggests an increase in the net magnetization (before switching occurs) as a function of the gate voltage (interestingly this is true for backward gate voltage sweep as well, where magnetization becomes increasingly negative). When the magnetic field/magnetization is reversed (traces 4, 5, 6), the magnetization versus voltage shows the opposite slope but the net magnetization (before switching) still generally increases during voltage sweeps. Such linear dependences were also measured in 2 other samples (5°- and 20°-tDB, Fig. S9), but the sign of the slope was opposite in the latter sample (20°-tDB, with generally decreasing magnetization magnitudes during voltage sweeps, Fig. S9f). These behaviors in response to voltage demonstrate intriguing electric field tuning of distinct time-reversal states (A, B states versus C, D states) in tDB CrI₃ as a result of different samples and initialization processes. The observed magnetoelectric (ME) effect may have two possible

origins. The electrostatic field can break the spatial-inversion symmetry of the layered magnet and create layer polarization of spin carriers^{17, 36, 38}. Furthermore, the gate voltage can effectively change the magnetic parameters of CrI₃^{27, 39} which could change the location of the system on the phase diagram below (Fig. 5) and hence modulate magnetization in twisted bilayers. The magnetoelectric effect can be quantified by the linear ME coefficient α_{zz} , defined as $\mu_0 \Delta M / 2t \equiv \alpha_{zz} E$, where $t \approx 0.7$ nm is the interlayer separation of CrI₃¹⁷, ΔM is the electric field-induced magnetization change, and E is the electric field. Since the MOKE signal for fully polarized spin states (high magnetic field in Fig. 4c) corresponds to the saturation magnetization ~ 0.137 mA per layer²⁷, we can extract $\Delta M/E$ from the slope in Fig. 4e (all six traces show similar slope values). For this sample we obtained $|\alpha_{zz}| \approx 32$ ps/m, which is of similar order of magnitude with the reported 110 ps/m for natural bilayer CrI₃¹⁷. Different slopes between different samples could arise from different locations and (voltage-swept) trajectories on the parameter space and phase diagram (Supplemental Section 9). The observed electrical tunability allows us to access and control the noncollinear magnetic states in tDB CrI₃.

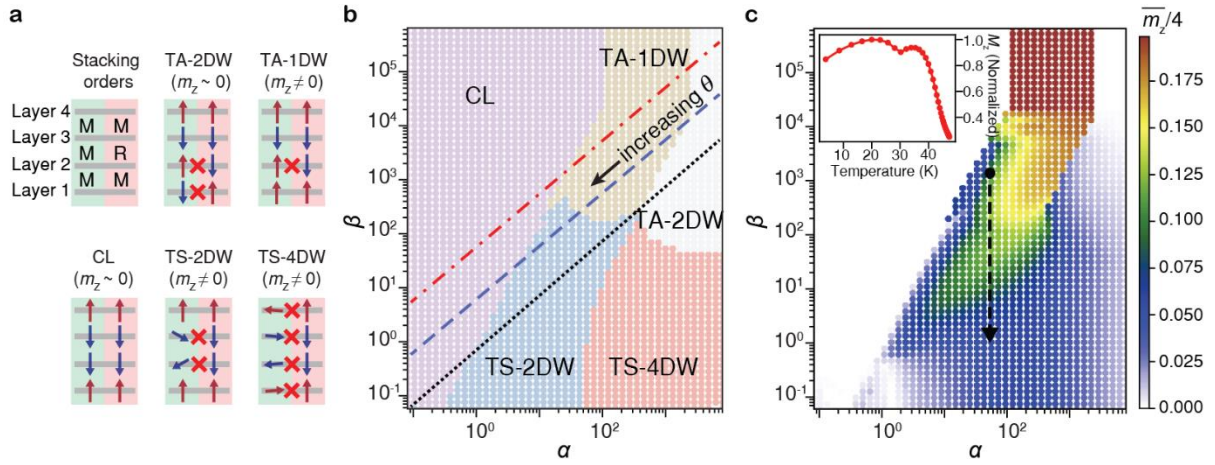


Figure 5 | Theoretical analysis of the moiré magnetism in tDB CrI₃. **a**, Schematics of the magnetic phases: twisted-A phase with double domain walls (TA-2DW), twisted-A phase with a single domain wall (TA-1DW), twisted-S phase with double domain walls (TS-2DW), twisted-S phase with four domain walls (TS-4DW), and collinear phase (CL, no domain walls). Layers 1-4 are labeled from bottom to top. Monoclinic (M) and rhombohedral (R) stacking are labeled for each layer pair (sandwiching the label) and M/R regions between the middle two layers are indicated by green/pink colors. Out-of-plane (in-plane) spins in the four layers are denoted by vertical (horizontal) arrows. The red crosses denote the magnetic domain walls where noncollinear spin textures exist. **b**, Magnetic phase diagram showing the emergence of noncollinear ground states as a function of dimensionless parameters α and β . Colored dots denote the simulated cases. The red dot-dashed, blue dashed, and black dotted lines correspond to constant K/J_{\perp}^0 ratios of 72.3, 7.23, and 0.723, respectively, suggesting phase transitions with the twist angle. **c**, Calculated net out-of-plane component of the dimensionless magnetization ($\overline{m_z}/4$) normalized by the value for fully spin-polarized states (i.e., out-of-plane spins $\uparrow\uparrow\uparrow$ in all layers gives $\overline{m_z}/4 = 1$) as a function of α and β . The dashed arrow is an exemplary trajectory of increasing temperature (T, starting from 7 K, with corresponding $(\alpha, \beta) = (56, 1230)$ marked by the black dot), giving a sharp drop in β and a nonmonotonic behavior of the overall out-of-plane physical magnetization M_z shown in the inset, for $\theta = 0.71^\circ$.

To better understand the observations, we theoretically study the moiré magnetism in tDB CrI₃. Within the continuum approximation²¹, the free energy per unit area for tDB CrI₃ with a relative twist between the middle two layers can be written as:

$$\mathcal{F}(\vec{m}_1, \vec{m}_2, \vec{m}_3, \vec{m}_4) = A \sum_{i=1}^4 (\nabla \vec{m}_i)^2 - K \sum_{i=1}^4 m_{iz}^2 + J_{\perp}^0 [\vec{m}_1 \cdot \vec{m}_2 + \Phi(\vec{r}) \vec{m}_2 \cdot \vec{m}_3 + \vec{m}_3 \cdot \vec{m}_4],$$

where \vec{m}_i is the position (\vec{r}) dependent unit vector oriented along the magnetization of layer i , A is the intralayer exchange stiffness, $K > 0$ is the easy axis anisotropy, and J_{\perp}^0 is the interlayer exchange constant for monoclinic stacking. $\Phi(\vec{r})$ accounts for the spatially-dependent interlayer exchange due to local variation of stacking between the twisted layers, which acts as a new degree of freedom tunable via the twist angle. The relative strengths of the intralayer, interlayer exchange and anisotropy energies determine the magnetic ground state of the system. Following the framework of Ref. ²¹, we define two dimensionless parameters $\alpha \equiv \frac{J_{\perp}^0}{Aq_m^2}$ and $\beta \equiv \frac{K}{Aq_m^2}$ that capture the relative strengths between these energy contributions, where $q_m = 1/L$ is the moiré wavevector.

Owing to the increased “layer degree of freedom” of the tDB system, a richer set of magnetic configurations beyond the twisted bilayer case^{10-12, 21, 24} is necessary to characterize the possible ground states of our system as functions of α and β . We schematically depict them in Fig. 5a (for convenience, we label the layers from bottom to top as 1, 2, 3, 4, and do not show the copies obtained by: (i) time reversal, or (ii) simultaneous swapping of the spin configurations between layers $1 \leftrightarrow 4$ and $2 \leftrightarrow 3$). When the configurations are governed by minimizing the free energy terms due to perpendicular anisotropy and interlayer exchange, the magnetization within each layer prefers to be primarily out-of-plane and have the interlayer spin orientations which minimize the *local* interlayer exchange (similar to the so-called twisted-A phase for twisted bilayer CrI₃²¹). For tDB CrI₃, the resultant configuration harbors $\sim 180^\circ$ domain walls (DW) in layers 1 and 2, which is referred to as the twisted-A double domain wall (TA-2DW) state. On the other hand, when the intralayer exchange energy cost associated with these DWs becomes more important, the system can reduce energy by getting rid of the DW in one or both layers, giving rise to configurations referred to as twisted-A one domain wall (TA-1DW) and collinear (CL) states, respectively. Since the area fraction of the R-stacking or FM (interlayer coupling between layers 2-3) region per moiré cell is larger than that of the M-stacking or AFM region (Supplementary Section 10.1), and the maximum strengths of the interlayer exchange of the FM and AFM regions are approximately the same, FM orientations between layers 2 and 3 is favored over AFM orientations for the CL state. Finally, similar to the bilayer CrI₃ case, for weaker perpendicular anisotropy, magnetic configurations with substantial in-plane components (the so-called twisted-S phase²¹) can be favored to lower the interlayer exchange energy via the formation of $\sim 90^\circ$ DWs. For tDB CrI₃, such $\sim 90^\circ$ DWs can be formed in the middle two layers or all the layers, resulting in configurations labeled as twisted-S two domain wall (TS-2DW) and twisted-S four domain wall (TS-4DW), respectively. By comparing the free energies of the abovementioned configurations (see Supplementary Section 10 for details), we present the phase diagram of ground states for the tDB CrI₃ system in Fig. 5b.

Equipped with the phase diagram, we next provide a qualitative understanding of the experimental observations. We begin by focusing on the twist angle dependence of MOKE. To this end, we show the trajectory of the corresponding magnetic phases traversed as the twist angle θ is increased. The three diagonal lines in Fig. 5b correspond to different parameter ratios K/J_{\perp}^0 . The blue dashed line corresponds to K, A and J_{\perp}^0 values extracted from the untwisted CrI₃ system^{40, 41}, while the red dot-dashed and black dotted lines are set at $\times 10$ and $\times 0.1$ of the original J_{\perp}^0 to allow for possible variation in parameters. Since the MOKE signal is proportional to perpendicular magnetization, in Fig. 5c, we also show the calculated

net out-of-plane magnetization component ($\overline{m_z}/4$) for different phases. For very small θ (i.e., large α and β), the TA-2DW state is the ground state. This is because the small θ implies the presence of large moiré domains (of size $\sim L\alpha a/\theta$) with varying signs of interlayer exchange. The system thus prefers to minimize the energy cost within the domains (at the expense of incurring intralayer exchange and anisotropy energy costs in the DWs) by choosing primarily out-of-plane magnetizations with interlayer arrangement following the sign of local interlayer exchange. Similar to the natural four-layer CrI₃, the TA-2DW phase carries negligible out-of-plane magnetization (Fig. 5c), consistent with the observed zero MOKE signal around zero twist angle, as shown in Fig. 2. With increasing twist angle θ , the domain wall energy (which increases proportionally to $L^{11,21}$) becomes comparable to the domain energy (which scales as L^2); the system thus makes a transition to the TA-1DW state, which, crucially, has a nonzero out-of-plane magnetization. Therefore, the observed MOKE signal going from 0 to finite values is consistent with the appearance of the TA-1DW state. As θ is further increased such that the cost of forming domain walls becomes too high, the system eventually collapses to a collinear phase (CL) with no DWs and vanishing net out-of-plane magnetization. This transition leads to a drop of the MOKE signal back to zero, as observed in Fig. 2. We remark that for smaller K/J_Λ^0 , the system can traverse through the twisted-S phases. However, to identify such noncollinear phases, other probes sensitive to in-plane magnetization are needed in future research, such as longitudinal MOKE or spatially sensitive spin probes^{10,42}.

Using the phase diagram, we also provide a possible explanation for the observed anomalous temperature dependence of the MOKE signal in Fig. 3. In addition to the twist angle, the temperature dependence of the magnetic properties (K , J_Λ^0 , and A) changes the relative strengths of the anisotropy, interlayer and intralayer exchange energies, resulting in a temperature-induced trajectory on the phase diagram. Depending on this trajectory and the starting phase, the overall out-of-plane physical magnetization ($M_z = \overline{m_z}M_s$) can *increase* with temperature before vanishing near the phase transition to the paramagnetic state. Here, M_s is the saturation magnetization. To demonstrate this possibility, we choose the twist angle of $\theta = 0.71^\circ$ (as for the device in Fig. 3), starting from $(\alpha, \beta) = (56, 1230)$ at low temperature (an exemplary choice of parameters within the red dot-dashed and black dotted lines mentioned above), and track the evolution of the system on the phase diagram as the temperature is increased. To this end, we vary K , J_Λ^0 , A and M_s according to the power law of temperature $\sim(1-T/T_c)^\gamma$, where T_c is the Curie temperature, with exponents γ that were experimentally obtained to be $\sim 2.3, 0.22, 0.22$ and 0.125 ^{11, 34, 35}. With increasing temperature (dashed arrow), $\overline{m_z}/4$ indeed shows an initial increase followed by a decrease in the phase diagram. Accordingly, we plot normalized M_z as a function of temperature (inset in Fig. 5c), showing the nonmonotonic temperature dependence, which is qualitatively consistent with our observations in Fig. 3c.

The qualitative agreement between the observations and theoretical results further supports the presence of rich noncollinear phases, as well as, their twist angle, temperature and voltage control in tDB CrI₃. We note, however, that quantitative differences exist, for example, in the critical twist angles for the transition between the phases (see Supplementary Section 10.2), and the functional forms of anomalous temperature dependence of MOKE. These differences could arise from the sensitivity of the phase diagram to material parameters, the presence of disorder^{10, 43}, or the trapping of experimentally observed spin configurations into metastable states.

In conclusion, we have demonstrated electrically tunable moiré magnetism in tDB CrI₃, whose emergent magnetic orders can be interpreted in the phase diagram associated with the moiré wavelength and magnetic parameters of the sample. The nontrivial magnetic phases potentially host topological skyrmion lattices²⁴ and magnon networks²³, which can be probed by spatially resolved measurements in future studies. Our findings also suggest that voltage is an effective knob to control magnetic orders with significant magnetic switching and magnetoelectric effect, leading to promising memory and spin-logic devices. As a novel degree of freedom, the twist can be applicable to the vast range of homo/heterobilayers of vdW magnets, including ferromagnets, antiferromagnets, multiferroics, and even quantum spin liquid candidates^{14, 44}, opening the opportunity to pursue new physics as well as spintronic applications.

Note added: During submission of this work, we became aware of a related preprint on twisted double bilayer CrI₃⁴⁵.

Methods

Crystal growth. Single crystal CrI₃ was synthesized using the chemical vapor transport (CVT) method⁴⁶. The Cr powder and iodine pieces were mixed with a stoichiometric ratio and loaded into a quartz tube (inner diameter, 10 mm; length, 180 mm). The quartz tube was sealed under vacuum and then transferred to a double-temperature-zone furnace. The temperatures of the hot and cold ends of the furnace were set at 650 °C and 550 °C, respectively. The growth with such a temperature gradient lasted for 7 days. Finally, the furnace was shut down, and the quartz tube was naturally cooled down to room temperature. The black plate-like CrI₃ crystals can be found at the cold end of the quartz tube.

Fabrication of twisted CrI₃ and gated devices. Flakes of CrI₃ were obtained by exfoliation of bulk material onto a silicon wafer with 285 nm oxide. The bilayers were selected by optical contrast and later confirmed by AFM and MOKE measurements. The tear-and-stack technique^{13, 28} was employed in this work to fabricate twisted double bilayers. We first used a polydimethylsiloxane/polycarbonate stamp to pick up an hBN flake. Then, we carefully controlled the hBN flake to contact one part of the selected bilayer CrI₃ flake. After lifting up the stamp, the contacting part of the CrI₃ flake was torn off by the hBN layer, and the remaining part was left on the silicon wafer. Then, the remaining part on the wafer was rotated with a target twist angle θ , aligned with the separated part on the hBN flake, and picked up to form the twisted stack. Afterwards, another hBN flake was picked up so the stacked CrI₃ layers were sandwiched between hBN and protected from degradation. Typical CrI₃ flakes before and after stacking are shown in Fig. 2a. To fabricate the back-gated device, few-layer graphene flakes were exfoliated and picked up during the stacking processes as the contact to tDB CrI₃. The stack was dropped onto prepatterned gold electrodes on a silicon wafer. The silicon oxide and bottom hBN flake act as back-gate dielectric layers. All exfoliation and stacking operations were performed inside an argon glovebox to avoid degradation. The exposure time to air was kept below ten minutes while transferring the fabricated sample into the sample chamber for measurements and pumping down.

TEM characterization. To fabricate TEM samples, very thin (<5 nm) top and bottom hBN flakes were used to improve the dark-field image contrast. The Holey silicon nitride support membrane can suspend the stack hBN/tDB CrI₃/hBN for TEM imaging. The twisted sample was characterized by scanning TEM equipped with a high angle annular dark-field (HAADF) detector on a ThermoFisher Scientific Themis Z Aberration-corrected Transmission Electron Microscope. The instrument was operated at 300 kV and 0.25 nA current.

Polar-MOKE microscopy. The polarization of linearly polarized light reflected from a magnetic material can be rotated by a Kerr angle θ_K , which is proportional to the magnetization of the material. In this work, the incident light is normal to the sample plane, and the MOKE is in the polar geometry, meaning that the

magnetic vector being probed is perpendicular to the sample surface and parallel to the incident light. A balanced photodetector and lock-in method are used to obtain the MOKE signal. A laser is used here with a wavelength of 633 nm and a power of 5 μ W. The sample is placed in a helium-flow optical cryostat with a temperature down to 6 K and magnetic field (perpendicular to the sample surface) up to 5 T. The laser is focused onto the sample surface by an objective with a spot diameter of 0.5 μ m. Note that in principle, the in-plane components of spins can emerge in twist magnets even with perpendicular magnetic anisotropy²¹. A perpendicular field induces canting of the in-plane spins (if any), giving rise to a continuously varying MOKE background⁴⁷, which is typically subtracted and eliminated from our MOKE signal. Therefore, we mainly focus on the out-of-plane components of spins with spin-flip transitions in this work.

Data availability

Data are available in the manuscript or supplementary materials. Additional data are available from the authors upon reasonable request.

Acknowledgements

We acknowledge partial support of the work from US Department of Energy (DOE) Office of Science through the Quantum Science Center (QSC, a National Quantum Information Science Research Center) and Department of Defense (DOD) Multidisciplinary University Research Initiatives (MURI) program (FA9550-20-1-0322) for materials and device fabrication and MOKE and TEM measurements. G.H.C. and Y.P.C. also acknowledges partial support from WPI-AIMR, JSPS KAKENHI Basic Science A (18H03858), New Science (18H04473 and 20H04623), and Tohoku University FRiDUO program in early stages of the research. M.R., A.R. and P.U. also acknowledge the support from the National Science Foundation (NSF) (ECCS-1810494). Z.Q.M. acknowledges the support by the US DOE under grant DE-SC0019068 for sample synthesis. K.W. and T.T. acknowledge support from the Elemental Strategy Initiative conducted by the MEXT, Japan (JPMXP0112101001) and JSPS KAKENHI (19H05790, 20H00354 and 21H05233).

Author contributions

G.H.C. and Y.P.C. conceived the project. G.H.C. fabricated the devices and performed experiments, assisted by A.L.A. M.M.R., A.R., and P.U. performed supporting theoretical analysis. X.T.L., G.H.C., L.L. and L.F. performed the TEM measurements. Y.L.Z. and Z.Q.M. provided bulk CrI₃ crystals. K.W. and T.T. provided bulk hBN crystals. Y.P.C. and P.U. supervised the project. G.H.C., M.M.R., P.U. and Y.P.C. wrote the manuscript with input from all co-authors.

Competing interests

The authors declare no competing financial interests.

Supplementary Information for

“Electrically tunable moiré magnetism in twisted double bilayer antiferromagnets”

Authors: Guanghui Cheng, Mohammad Mushfiqur Rahman, Andres Llacsahuanga Allcca, Avinash Rustagi, Xingtao Liu, Lina Liu, Lei Fu, Yanglin Zhu, Zhiqiang Mao, Kenji Watanabe, Takashi Taniguchi, Pramey Upadhyaya*, Yong P. Chen*

*Correspondence to: prameyup@purdue.edu; yongchen@purdue.edu

1. Fabrication and atomic force microscopy characterization of tDB CrI₃

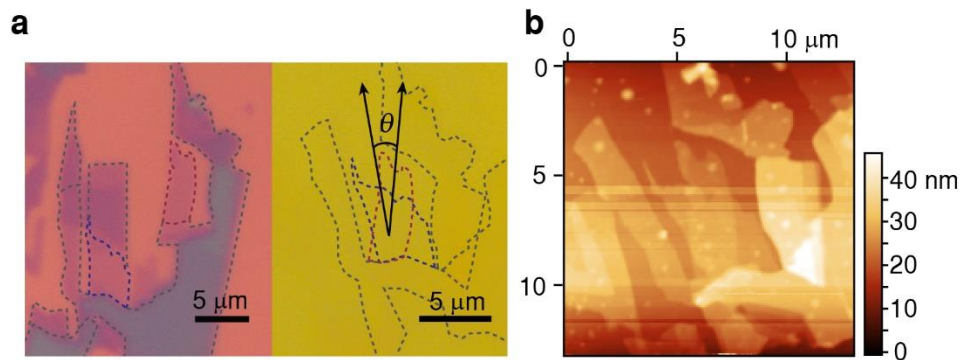


Figure S1 | **a**, Optical micrograph of a representative tDB CrI₃ before and after stacking. The top and bottom CrI₃ bilayers are outlined by the blue and red dashed lines, respectively. Thicker CrI₃ flakes are outlined by gray dashed lines. Although the blue and red parts do not directly adjoin each other, they are connected by the thick part, therefore sharing the same crystal orientation. **b**, Atomic force microscopy image of the same tDB CrI₃ sample as in **a** shows a uniform stacking interface with few bubbles. The horizontal lines are the scanning glitches.

2. STEM characterizations of bilayer CrI₃ and tDB CrI₃

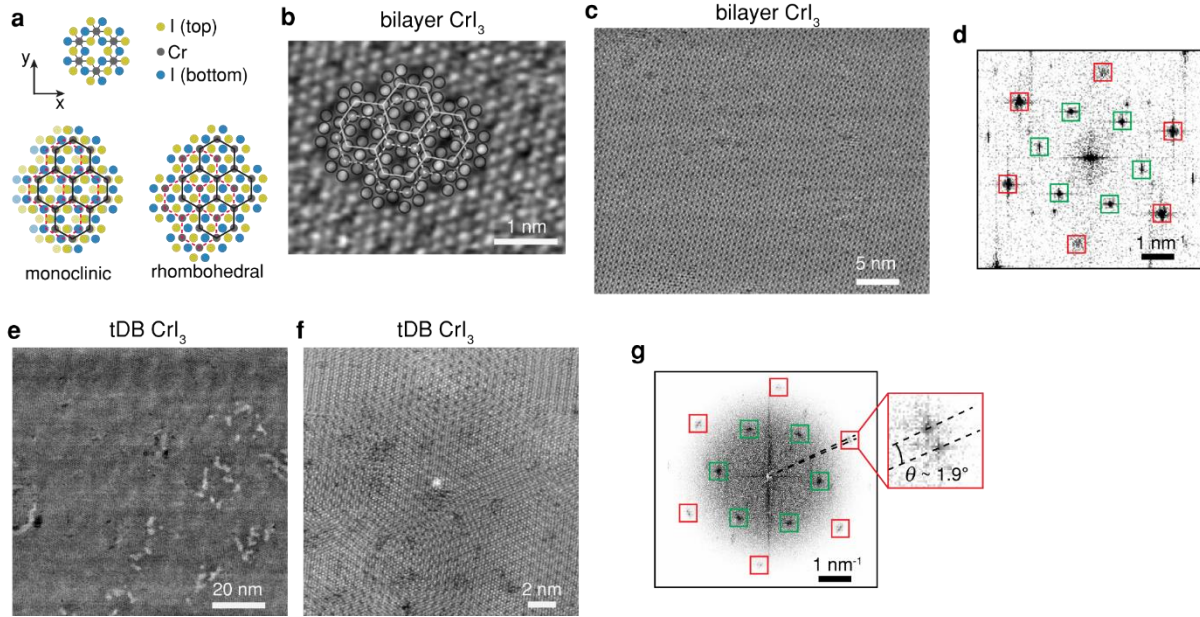


Figure S2 | **a**, Schematics of the monoclinic and rhombohedral structures of bilayer CrI_3 . The black solid and red dashed lines connect the Cr atoms of the top layer and bottom layer, respectively. **b-d**, Atomic-resolution STEM images and fast Fourier transform (FFT) pattern of bilayer CrI_3 (from the same CrI_3 flake as for the twist region in **e-h**). The atomic registry outlined by the circles and lines suggests a monoclinic stacking structure. Green and red rectangles mark the first- and second-order Bragg peaks with sixfold rotation symmetry, respectively. **e,f**, Atomic-resolution STEM images and FFT pattern of tDB CrI_3 with a target angle of 0.142° . The white patches in the STEM image are radiation-induced damage by the electron beam. Similar to bilayer CrI_3 , green and red rectangles mark the first- and second-order Bragg peaks, respectively. Remarkably, the magnification of one peak shows two slightly separated peaks originating from the top and bottom bilayer CrI_3 with a measured twist angle of 1.9° , within the accuracy $\sim \pm 0.5^\circ$ of the stacking processes. The moiré wavelength can be estimated to be $L = \frac{a}{2\sin(\theta/2)} \sim 20.5 \text{ nm}$, where a is the lattice constant of $\text{CrI}_3 \sim 0.682 \text{ nm}^2$.

3. MOKE results of natural four-layer CrI_3

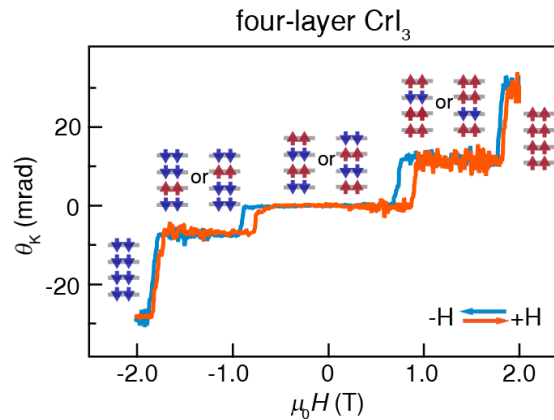


Figure S3 | MOKE signal of a natural four-layer CrI₃ as a function of a perpendicular magnetic field up to 2 T. The interlayer AFM coupling in natural four-layer CrI₃ leads to zero net magnetization at zero field³². Insets depict magnetic ground states.

4. MOKE results of tDB CrI₃ with different twist angles

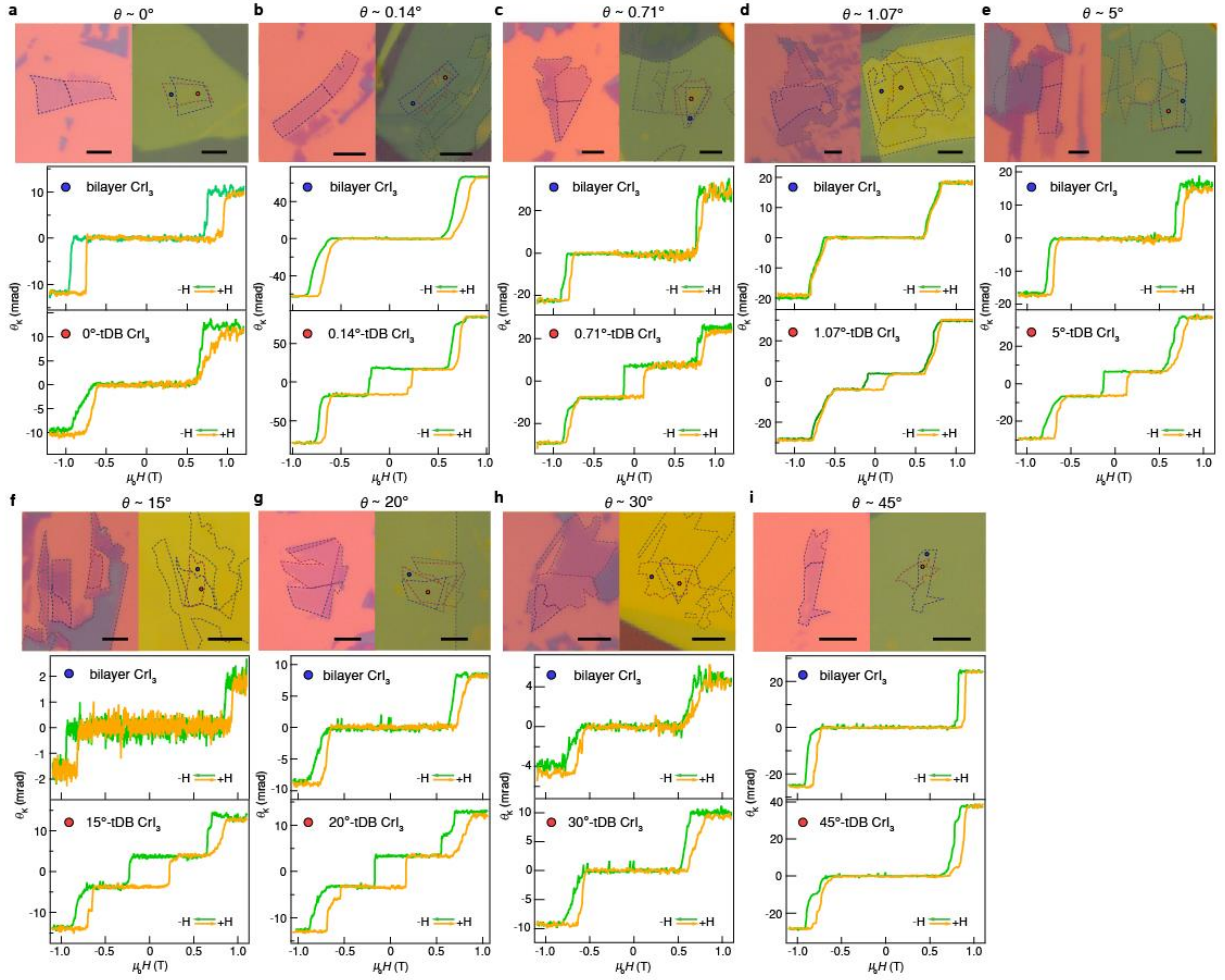


Figure S4 | MOKE signal as a function of the perpendicular magnetic field in bilayer CrI₃ and tDB CrI₃ with different twist angles (each from the same CrI₃ flake). a-i, Optical micrographs on top of each MOKE result show the bilayer CrI₃ flake (left) and tDB CrI₃ (right) made from it by the tear-and-stack technique. The top and bottom CrI₃ bilayers are outlined by the blue and red dashed lines, respectively. Thicker flakes or other materials are outlined by gray dashed lines. The MOKE signals in bilayer CrI₃ and tDB CrI₃ are obtained at the blue and red spots denoted in each sample image. Scale bars are 5 μm.

5. MOKE results of tDB CrI₃ under high fields

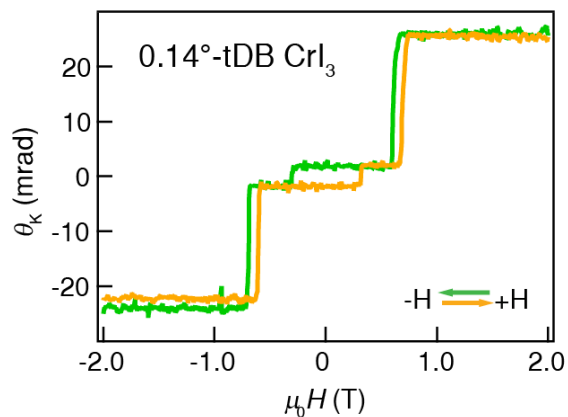


Figure S5 | MOKE signal as a function of perpendicular magnetic field up to 2 T in a 0.14°-tDB CrI₃. Data obtained from the same sample as in Fig. 4. The different magnitudes of the MOKE signal from that in Fig. 4 are due to different measuring spots related to the sample nonuniformity.

6. Uniformity check of the magnetic behaviors in tDB CrI₃

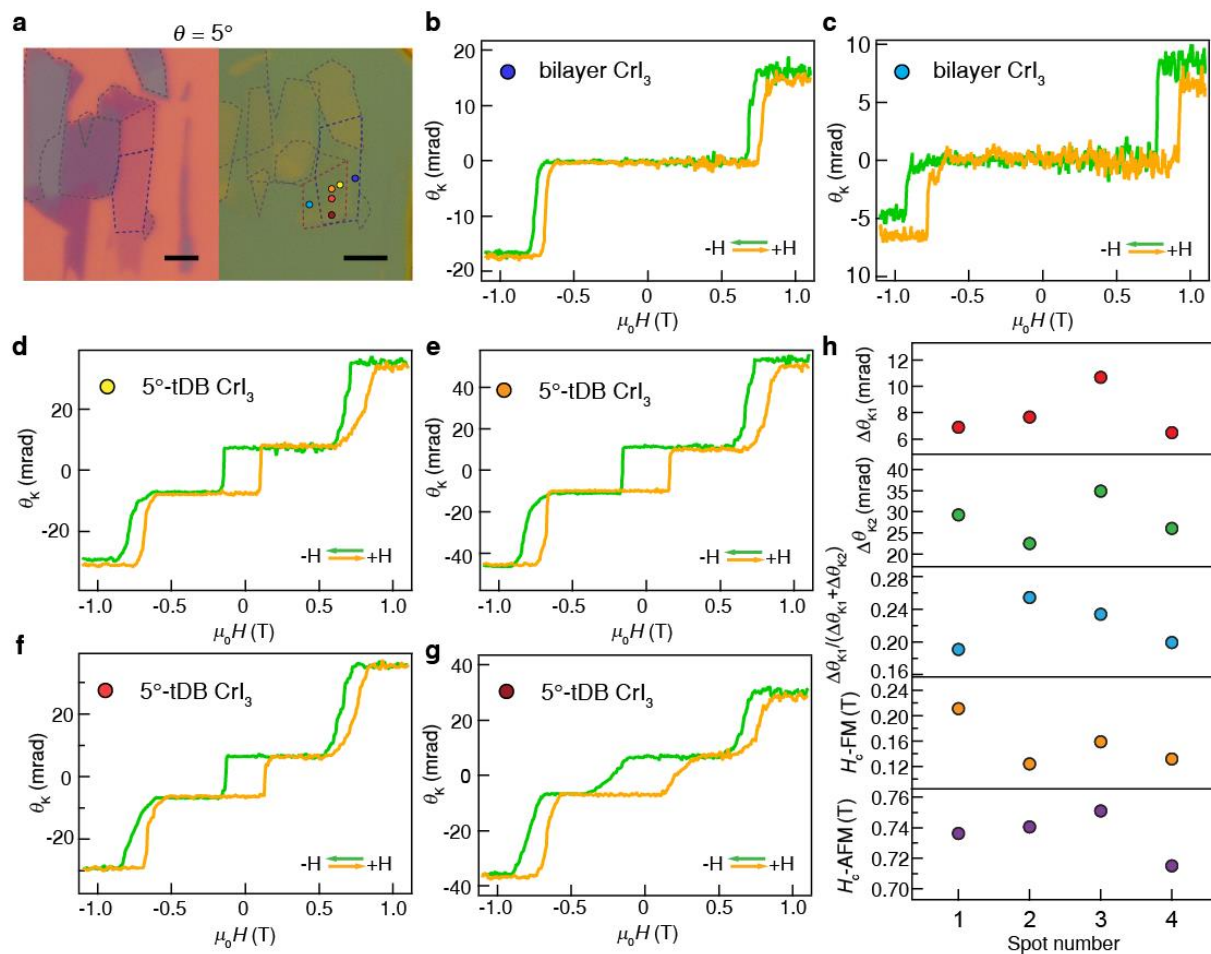


Figure S6 | **a**, Optical micrograph of a bilayer CrI₃ flake (left) and a 5°-tDB CrI₃ (right) made from it. The top and bottom bilayers CrI₃ are outlined by the blue and red dashed lines, respectively. Thicker flakes are outlined by gray dashed lines. Scale bars are 5 μm. **b-g**, MOKE signal as a function of magnetic field obtained in different positions denoted by color spots in **a**, indicating the spatial nonuniformity of the sample. One possible reason is that CrI₃ layers are more fragile and softer than graphene and transition metal dichalcogenides and therefore sensitive to local strain or disorder¹⁰. The lattice reconstruction for twisted systems^{10, 48} may also contribute to the structural distortion, affecting the uniformity of its magnetism. **h**, Uniformity check for typical parameters of spots 1-4 in the 5°-tDB CrI₃ region, corresponding to MOKE results in **d-g**. The parameters include MOKE magnitudes of the FM loop $\Delta\theta_{K1}$ and AFM transition $\Delta\theta_{K2}$, the fraction of FM loop MOKE magnitudes $\Delta\theta_{K1}/(\Delta\theta_{K1}+\Delta\theta_{K2})$, transition fields of FM coercivity H_c -FM and AFM spin-flip H_c -AFM.

7. Dependence of transition fields on the twist angle

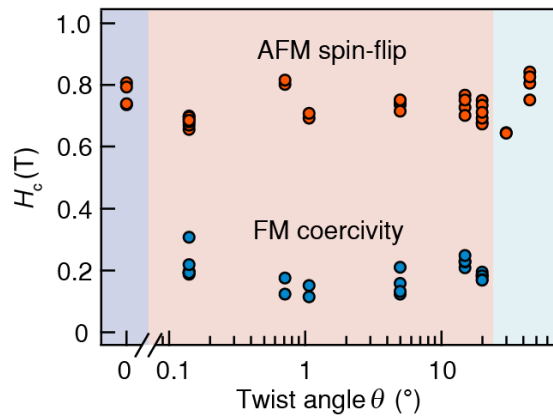


Figure S7 | Transition fields H_c of FM coercivity and AFM spin-flip as a function of the twist angle. For twist angles of 0° or above 20°, only H_c of AFM spin-flip is shown due to the disappearance of FM loops.

8. Representative MOKE curves at different gate voltages

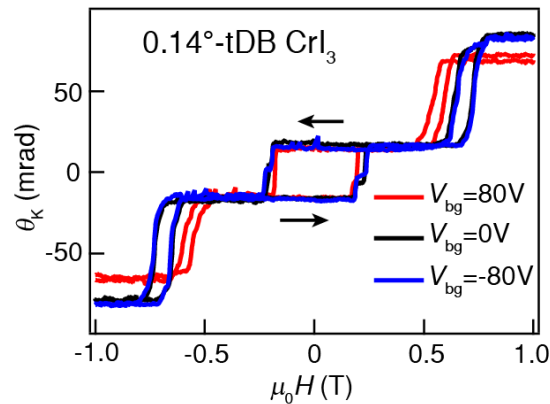


Figure S8 | MOKE signal as a function of the perpendicular magnetic field in 0.14°-tDB CrI₃ at three representative back-gate voltages for the device shown in Fig. 4. Two curves of each voltage represent forward and backward sweeps of the field.

9. Voltage-assisted magnetic switching for other twist angles

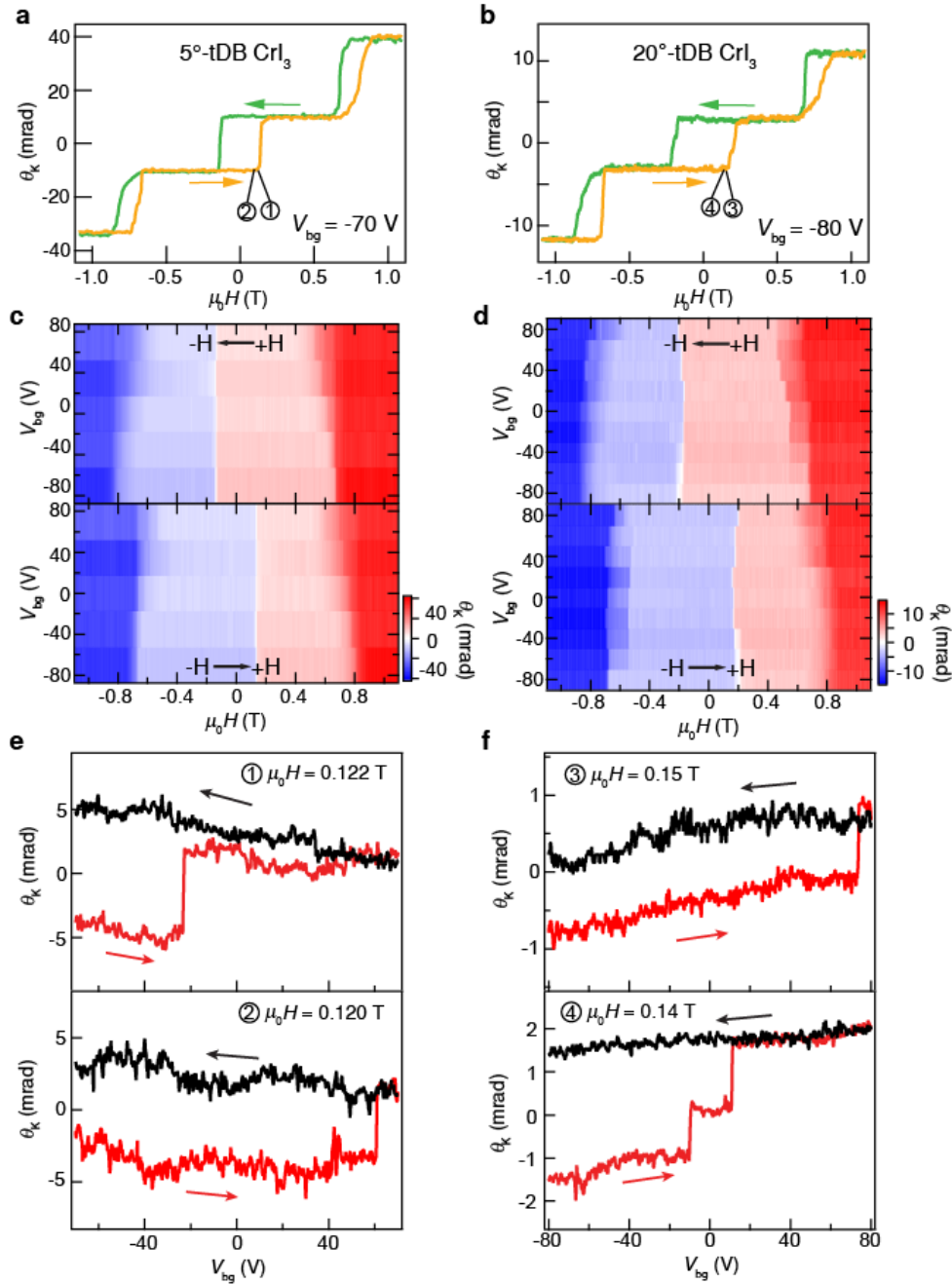


Figure S9 | Voltage-assisted magnetic switching in 5°-tDB CrI₃ and 20°-tDB CrI₃. **a,b**, MOKE signal as a function of magnetic field at gate voltages of -70V and -80V in 5°- and 20°-tDB CrI₃, respectively. Field sweeping directions are denoted by the arrows. **c,d**, MOKE signal as a function of magnetic field and back-gate voltage. The top and bottom panels correspond to backward and forward sweeps of the magnetic field, respectively. The sharp color boundaries indicate the FM coercivity and AFM spin-flip transitions. **e,f**, MOKE signal as a function of the back-gate voltage in 5°- and 20°-tDB CrI₃, respectively. Voltage sweeping directions are denoted by the arrows. The samples are initialized in the fully polarized states by a high magnetic field of -1.1 T and then biased at fields of ① 0.122 T, ② 0.120 T, ③ 0.15 T, ④ 0.14 T, respectively, corresponding to the circled numbers in **a,b**. Similar to 0.14°-tDB CrI₃ in Fig. 4, the magnetoelectric effect is also observed in **e** ($\theta \sim 5^\circ$) and in **f** ($\theta \sim 20^\circ$). The linear ME coefficients can be

extracted to be $|\alpha_{zz}| \approx 37$ ps/m and 8 ps/m for 5°- and 20°-tDB CrI₃, respectively. Interestingly, we note the magnetoelectric effect in the 20°-tDB (Fig. S9f) has “opposite trend” from the two samples with much smaller twisting angles (5°-tDB, Fig. S9e, and 0.14°-tDB, Fig. 4e lower 3 panels) measured under otherwise similar conditions: the signs of the slope (or α_{zz}) of magnetoelectric effect are opposite, and when biased at larger (closer to coercive) magnetic fields the 20°-tDB switches *later* during the voltage sweep whereas the 5°-tDB and 0.14°-tDB switch earlier. Such different behaviors apparently between samples with different twisting angles may arise from their different locations on the phase diagram (Fig. 5, even possibly with their low field states such as A belonging to different noncollinear phases) and different voltage-tuned parameters and trajectories, and are subjects for future investigations to better understand.

10. Continuum analysis of twisted double bilayer CrI₃

In this section, we carry out micromagnetic simulations to study the noncollinear moiré magnetism in twisted double bilayer (tDB) CrI₃. We find that a collection of magnetic phases can be stabilized due to the competition between various magnetic interactions, namely, anisotropy, intralayer and interlayer exchange energies. To this end, we use the mumax3 package⁴⁹ to numerically solve the LLG equation to find the magnetic ground states.

The interlayer exchange coupling in CrI₃ has a one-to-one correspondence with the interlayer stacking orders. For example, monoclinic stacking favors AFM coupling, while rhombohedral stacking favors FM coupling²⁵. A relative twist angle between any two neighboring layers creates spatially periodic distributions of monoclinic (M) and rhombohedral (R) stacking regions, subjecting the system to competing energy interactions. As we argue next, the relative strength of the energy cost of forming magnetic domain walls (DWs) and the energy gain from magnetic domains, as dictated by the local interlayer exchange, determine the ground state of such a system.

Based on our experimental configuration and other relevant studies^{10-12, 21, 24}, we consider here a four-layer CrI₃ system with a twist angle between the middle two layers. The top and bottom bilayers retain a naturally monoclinic stacking order. The DW energy cost scales with L/a , and the magnetic domain energy gain scales with $(L/a)^2$ ^{11, 21}, where L is the moiré wavelength (also the length scale of the stacking and magnetic domains) and a is the lattice constant. For small twist angles, we have $(L/a)^2 > L/a$, indicating that the system can minimize its energy with magnetizations following the local interlayer stacking orders at the cost of domain walls established between magnetic domains. We regard this state as the twisted-A phase with two domain walls (TA-2DW)²¹. The spin textures are shown in Fig. 5a. As we start increasing the twist angle (and consequently decreasing L), the DW energies become comparable to the domain energies, forcing the system to reduce the DWs to minimize the DW energies. Due to the maximum interlayer FM and AFM exchange coupling between the twisted layers being substantially stronger than AFM exchange in natural bilayer M stacking^{11, 25}, the cost of forming DW in layers 2 and 3 is smaller than that in layers 1 and 4 (in other words, if the system were to eliminate a DW it would prefer to eliminate one in layer 1 or 4 and violate the AFM coupling in natural bilayer 1-2 or 3-4 rather than to eliminate one in layer 2 or 3). Therefore, we expect the twisted-A phase with a single domain wall (TA-1DW) to emerge where the DW is in layer 2 or 3. The system can further minimize its DW energy by forming 90° domain walls (i.e., an in-plane spin texture in one of the neighboring domains). Due to the competing interactions between interlayer exchange and anisotropy, the system energy for lower K/J_{\perp}^0 is minimized by forming 90° DWs. We refer to these states as twisted-S phases (TS-2DW and TS-4DW)²¹. The energy loss from having in-plane spin configurations is balanced by the energy gain from reducing the DW width by half. Finally, as θ is further

increased beyond a critical angle such that the cost of forming domain walls becomes too high, we expect the system to collapse to a collinear phase (CL). Based on the above preliminary analysis, we use these states as ansatzes and search for the minimum energy states among them as a function of the physical parameters.

10.1 Spatial distribution of the moiré magnetism

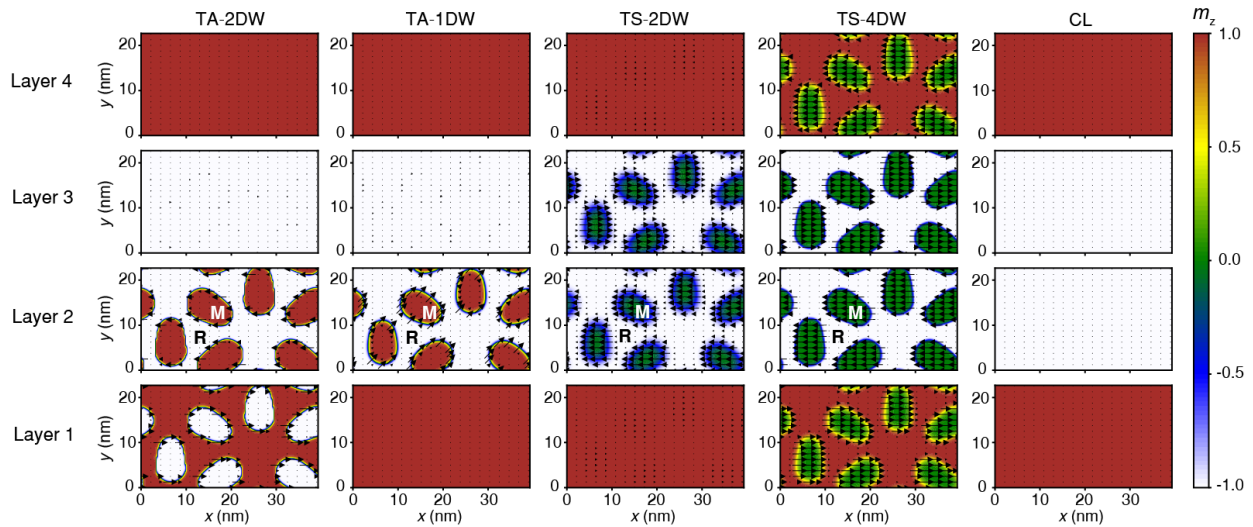


Figure S10 | Theoretical analysis of the moiré magnetism in tDB CrI₃. Spatial distribution of out-of-plane magnetization in each of the four layers of the TA-2DW, TA-1DW, TS-2DW, TS-4DW, and CL phases. The regions with M and R stacking between the twisted layers are marked. The spatial profile of the interlayer exchange between the twisted layers was constructed by fitting DFT results²⁵ taking up to five harmonics in the reciprocal lattice space. The arrows indicate the in-plane magnetization components.

Figure S10 shows the simulated spatial distribution of the out-of-plane magnetization (along with the in-plane components shown by arrows) in each of the four layers for the TA-2DW, TA-1DW, TS-2DW, TS-4DW, and CL phases. The magnetization textures in the twisted middle two layers of the noncollinear phases verify the expected periodic magnetic domains and domain walls arising from the moiré superlattice-modulated interlayer exchange in tDB CrI₃. Note that the R-stacking or FM region is larger in area fraction than the M-stacking or AFM region, and a direct summation over the real space of the spatial profile function $\Phi(\vec{r})$ reveals that the interlayer energy contribution from the FM regions is stronger than that of AFM regions for nonzero twist angles. This is consistent with the observed FM order in the case of monolayer-on-monolayer twisted structures^{11, 21} at high twist angles.

10.2 Analysis of the critical twist angles and the sensitivity to sample parameters

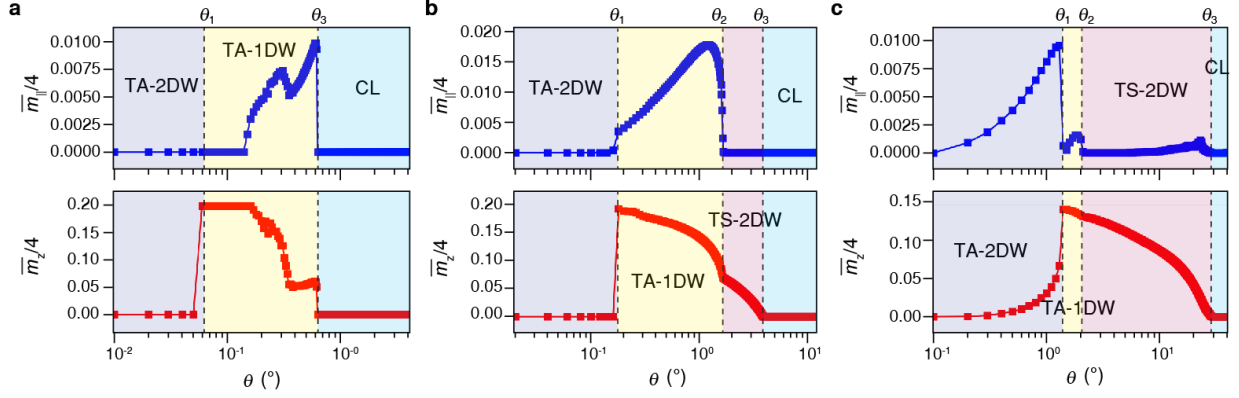


Figure S11 | The net calculated in-plane (upper panels) and out-of-plane (lower panels) components of the total magnetization as a function of twist angle θ , calculated via micromagnetic simulations for $K = 0.256$ erg/cm² and different interlayer exchange strengths $J_{\perp}^0 = 0.00354$ erg/cm² (a), $J_{\perp}^0 = 0.0354$ erg/cm² (b), and $J_{\perp}^0 = 0.354$ erg/cm² (c), corresponding to the 3 (red, blue, and black) dashed/dotted diagonal lines in Fig. 5b. The critical angles are denoted by θ_1 , θ_2 , θ_3 and dashed lines.

Next, we calculate the critical twist angles for the above magnetic phases for a given choice of material parameters. The magnetic phases are stabilized by the relative strengths of the respective energy contributions to the free energy. The twist angle θ modulates the moiré periodicity, thus providing a control knob to tune the moiré wavevector (q_m) and parameters (α, β). As a result, upon adjusting the twist angle, one traverses diagonally in the phase diagram following a constant K/J_{\perp}^0 line (Fig. 5b) and stabilizes various magnetic phases. In Fig. S11, we plot the net calculated out-of-plane (in-plane) component of the total magnetization \overline{m}_z (\overline{m}_{\parallel}) normalized by the fully spin-polarized states (i.e., out-of-plane spins $\uparrow\uparrow\uparrow\uparrow$ in all layers give $\overline{m}_z/4 = 1$, while in-plane spins $\rightarrow\rightarrow\rightarrow\rightarrow$ give $\overline{m}_{\parallel}/4 = 1$) as a function of the twist angle θ . Figure S11b shows the plot based on typical experimental parameters for untwisted CrI₃^{40, 41}, corresponding to the blue dashed line in Fig. 5b. Physically, for small θ , domain walls are energetically less expensive compared to uncompensated domains, forcing the system to relax to the TA-2DW phase with negligible net magnetization. With increasing θ , we find that $\overline{m}_z/4$ stays close to zero until a sharp rise to its maximum value at a critical angle θ_1 . The small increase in $\overline{m}_{\parallel}/4$ near θ_1 is a consequence of shrinking domain areas, which provides a way to minimize the system energy by reducing the DW length. Beyond θ_1 , the system first eliminates one of the domain walls that leads to a nonzero out-of-plane magnetization, which we refer to as the TA-1DW phase. The system can further minimize its energy by forming an in-plane AFM-coupled spin configuration called the TS phases below a certain β . Thus, at θ_2 , a transition from TA-1DW to TS-2DW takes place. Finally, the TS-2DW phase transitions to the CL phase at θ_3 , as indicated by the vanishing out-of-plane magnetization $\overline{m}_z/4$. This overall trend qualitatively agrees with the observed twist angle dependence of the MOKE signal in Fig. 2f.

The critical angles for the phase transitions are quite sensitive to the sample parameters. Using the typical experimental parameters for untwisted CrI₃ $K = 0.256$ erg/cm², $J_{\perp}^0 = 0.0354$ erg/cm², and $A = 2.29 \times 10^{-15}$ erg^{40, 41}, we have $\beta/\alpha = K/J_{\perp}^0 = 7.23$ (blue dashed line in Fig. 5b), and the critical angles are estimated to

be $\theta_1 \approx 0.2^\circ$, $\theta_2 \approx 1.15^\circ$ and $\theta_3 \approx 3.6^\circ$ (Fig. S11b). However, just by scaling the parameter J_\perp^0 up (down) by one order of magnitude, we obtain (the upper critical angle above which $\overline{m_z}/4$ drops to 0 again) $\theta_3 \approx 27^\circ$ ($\theta_3 \approx 0.6^\circ$), as shown in Figs. S11c,a, corresponding to the red and black dashed lines in Fig. 5b. Under the selected parameters, it can even avoid traversing some of the five phases. For instance, the red dashed line in Fig. 5b indicates transitions through TA-2DW \rightarrow TA-1DW \rightarrow CL phases, whereas for the black dashed line, we find transitions of TA-2DW \rightarrow TA-1DW \rightarrow TS-2DW \rightarrow CL phases. To the lower right side of the black dashed line, we expect transitions through TA-2DW \rightarrow TS-4DW \rightarrow TS-2DW \rightarrow CL phases, with small out-of-plane net magnetization. Such sensitivity to sample parameters provides a possible reason for the different experimental results in the twisted CrI₃ system¹⁰⁻¹².

References

1. Cao, Y. et al. Correlated insulator behaviour at half-filling in magic-angle graphene superlattices. *Nature* **556**, 80-84 (2018).
2. Cao, Y. et al. Unconventional superconductivity in magic-angle graphene superlattices. *Nature* **556**, 43-50 (2018).
3. Jin, C. et al. Observation of moiré excitons in WSe₂/WS₂ heterostructure superlattices. *Nature* **567**, 76-80 (2019).
4. Chen, G. et al. Evidence of a gate-tunable Mott insulator in a trilayer graphene moiré superlattice. *Nat. Phys.* **15**, 237-241 (2019).
5. Hunt, B. et al. Massive Dirac fermions and Hofstadter butterfly in a van der Waals heterostructure. *Science* **340**, 1427-1430 (2013).
6. Sharpe, A. L. et al. Emergent ferromagnetism near three-quarters filling in twisted bilayer graphene. *Science* **365**, 605-608 (2019).
7. Sunku, S. S. et al. Photonic crystals for nano-light in moiré graphene superlattices. *Science* **362**, 1153-1156 (2018).
8. Chen, X. et al. Moiré engineering of electronic phenomena in correlated oxides. *Nat. Phys.* **16**, 631-635 (2020).
9. Hu, G. et al. Topological polaritons and photonic magic angles in twisted α -MoO₃ bilayers. *Nature* **582**, 209-213 (2020).
10. Song, T. et al. Direct visualization of magnetic domains and moiré magnetism in twisted 2D magnets. *Science* **374**, 1140-1144 (2021).
11. Xu, Y. et al. Coexisting ferromagnetic–antiferromagnetic state in twisted bilayer CrI₃. *Nat. Nanotechnol.* **17**, 143-147 (2021).
12. Xie, H. et al. Twist engineering of the two-dimensional magnetism in double bilayer chromium triiodide homostructures. *Nat. Phys.* **18**, 30–36 (2021).
13. Cao, Y. et al. Superlattice-induced insulating states and valley-protected orbits in twisted bilayer graphene. *Phys. Rev. Lett.* **117**, 116804 (2016).
14. Burch, K. S. Mandrus, D. & Park, J. G. Magnetism in two-dimensional van der Waals materials. *Nature* **563**, 47-52 (2018).
15. Banerjee, A. et al. Neutron scattering in the proximate quantum spin liquid α -RuCl₃. *Science* **356**, 1055-1058 (2017).
16. Gibertini, M. Koperski, M. Morpurgo, A. F. & Novoselov, K. S. Magnetic 2D materials and heterostructures. *Nat. Nanotechnol.* **14**, 408-419 (2019).
17. Jiang, S. W. Shan, J. & Mak, K. F. Electric-field switching of two-dimensional van der Waals magnets. *Nat. Mater.* **17**, 406-410 (2018).

18. Li, T. X. et al. Pressure-controlled interlayer magnetism in atomically thin CrI₃. *Nat. Mater.* **18**, 1303-1308 (2019).
19. Deng, Y. et al. Gate-tunable room-temperature ferromagnetism in two-dimensional Fe₃GeTe₂. *Nature* **563**, 94-99 (2018).
20. Gong, C. et al. Discovery of intrinsic ferromagnetism in two-dimensional van der Waals crystals. *Nature* **546**, 265-269 (2017).
21. Hejazi, K. Luo, Z. X. & Balents, L. Noncollinear phases in moiré magnets. *Proc. Natl. Acad. Sci. U.S.A.* **117**, 10721-10726 (2020).
22. Tong, Q. J. Liu, F. Xiao, J. & Yao, W. Skyrmions in the moiré of van der Waals 2D magnets. *Nano Lett.* **18**, 7194-7199 (2018).
23. Wang, C. Gao, Y. Lv, H. Y. Xu, X. D. & Xiao, D. Stacking domain wall magnons in twisted van der Waals magnets. *Phys. Rev. Lett.* **125**, 247201 (2020).
24. Akram, M. LaBollita, H. Dey, D. Kapeghian, J. Erten, O. & Botana, A. S. Moiré skyrmions and chiral magnetic phases in twisted CrX₃ (X = I, Br, and Cl) bilayers. *Nano Lett.* **21**, 6633-6639 (2021).
25. Sivadas, N. Okamoto, S. Xu, X. D. Fennie, C. J. & Xiao, D. Stacking-dependent magnetism in bilayer CrI₃. *Nano Lett.* **18**, 7658-7664 (2018).
26. Wang, W.-G. Li, M. Hageman, S. & Chien, C. L. Electric-field-assisted switching in magnetic tunnel junctions. *Nat. Mater.* **11**, 64-68 (2012).
27. Jiang, S. W. Li, L. Z. Wang, Z. F. Mak, K. F. & Shan, J. Controlling magnetism in 2D CrI₃ by electrostatic doping. *Nat. Nanotechnol.* **13**, 549-553 (2018).
28. Kim, K. et al. Van der Waals heterostructures with high accuracy rotational alignment. *Nano Lett.* **16**, 1989-1995 (2016).
29. Wu, M. Li, Z. L. Cao, T. & Louie, S. G. Physical origin of giant excitonic and magneto-optical responses in two-dimensional ferromagnetic insulators. *Nat. Commun.* **10**, 2371 (2019).
30. Andrei, E. Y. & MacDonald, A. H. Graphene bilayers with a twist. *Nat. Mater.* **19**, 1265-1275 (2020).
31. Huang, B. et al. Layer-dependent ferromagnetism in a van der Waals crystal down to the monolayer limit. *Nature* **546**, 270-273 (2017).
32. Song, T. C. et al. Giant tunneling magnetoresistance in spin-filter van der Waals heterostructures. *Science* **360**, 1214-1218 (2018).
33. Lu, X. Fei, R. & Yang, L. Curie temperature of emerging two-dimensional magnetic structures. *Phys. Rev. B* **100**, 205409 (2019).
34. Kohlhepp, J. Elmers, H. J. Cordes, S. & Gradmann, U. Power laws of magnetization in ferromagnetic monolayers and the two-dimensional Ising model. *Phys. Rev. B* **45**, 12287-12291 (1992).
35. Kim, M. et al. Micromagnetometry of two-dimensional ferromagnets. *Nat. Electron.* **2**, 457-463 (2019).
36. Huang, B. et al. Electrical control of 2D magnetism in bilayer CrI₃. *Nat. Nanotechnol.* **13**, 544-548 (2018).
37. Chiba, D. Yamanouchi, M. Matsukura, F. & Ohno, H. Electrical Manipulation of Magnetization Reversal in a Ferromagnetic Semiconductor. *Science* **301**, 943-945 (2003).
38. Sivadas, N. Okamoto, S. & Xiao, D. Gate-controllable magneto-optic Kerr effect in layered collinear antiferromagnets. *Phys. Rev. Lett.* **117**, 267203 (2016).
39. Lei, C. Chittari, B. L. Nomura, K. Banerjee, N. Jung, J. & MacDonald, A. H. Magnetoelectric response of antiferromagnetic CrI₃ bilayers. *Nano Lett.* **21**, 1948-1954 (2021).
40. Lado, J. L. & Fernández-Rossier, J. On the origin of magnetic anisotropy in two dimensional CrI₃. *2D Mater.* **4**, 035002 (2017).
41. Rustagi, A. Solanki, A. B. Tserkovnyak, Y. & Upadhyaya, P. Coupled spin-charge dynamics in magnetic van der Waals heterostructures. *Phys. Rev. B* **102**, 094421 (2020).

42. Du, C. et al. Control and local measurement of the spin chemical potential in a magnetic insulator. *Science* **357**, 195-198 (2017).
43. Sun, Q. C. et al. Magnetic domains and domain wall pinning in atomically thin CrBr₃ revealed by nanoscale imaging. *Nat. Commun.* **12**, 1989 (2021).
44. Gong, C. & Zhang, X. Two-dimensional magnetic crystals and emergent heterostructure devices. *Science* **363**, eaav4450 (2019).
45. Xie, H. et al. Evidence of noncollinear spin texture in magnetic moiré superlattices. *arXiv preprint*, arXiv:2204.01636 (2022).
46. Liu, Y. & Petrovic, C. Three-dimensional magnetic critical behavior in CrI₃. *Phys. Rev. B* **97**, 014420 (2018).
47. Cai, X. et al. Atomically thin CrCl₃: an in-plane layered antiferromagnetic insulator. *Nano Lett.* **19**, 3993-3998 (2019).
48. Yoo, H. et al. Atomic and electronic reconstruction at the van der Waals interface in twisted bilayer graphene. *Nat. Mater.* **18**, 448-453 (2019).
49. Vansteenkiste, A. Leliaert, J. Dvornik, M. Helsen, M. Garcia-Sanchez, F. & Van Waeyenberge, B. The design and verification of MuMax3. *AIP Adv.* **4**, 107133 (2014).